Unraveling the Effect of Binary Metal Fluoride in Tin Perovskite Solar Cells

Aman Shukla[1,2‡], Mai Otake[3], Masatoshi Yanagida[1], Koichi Yamashita[3], Azusa Muraoka[3] *, Yasihiro Shirai[1], Dhruba B. Khadka[1‡] *

[1]*Photovoltaic Materials Group, Center for GREEN Research on Energy and Environmental Materials, National Institute for Materials Science (NIMS), 1-1 Namiki, Tsukuba, Ibaraki 305-0044, Japan.*

[2]*Department of Materials Science & Engineering, National Centre for Flexible Electronics, Indian Institute of Technology Kanpur, Kanpur, Uttar Pradesh 208016, India.*

[3]*Graduate School of Science, Japan Women's University, 2-8-1, Mejirodai, Bunkyo-ku, Tokyo, 112-8681, Japan.*

Corresponding Author

*E-mail: DBK: KHADKA.B.Dhruba@nims.go.jp

*AM: muraokaa@fc.jwu.ac.jp

‡These authors contributed equally to this work.

Abstract

Tin-based perovskite solar cells (PSCs) are promising lead-free photovoltaic candidates, but their performance is limited by Sn^{2+} oxidation, high defect density, and severe self-p-doping. Here, we employ fluoride-based additive engineering using BaF_2, SrF_2, and YbF_3 to regulate the crystallization, defect chemistry, and electronic structure of $FASnI_3$ perovskites. Among the investigated additives, SrF_2 delivers the best device performance, increasing the power conversion efficiency from 9.7% to 12.7% with enhanced operational stability. Density functional theory calculations reveal that all dopants suppress Sn off-centering and reduce electron effective-mass anisotropy, although their structural and electronic effects differ significantly. Ba doping exhibits the most favorable thermodynamic stability, while Yb doping most effectively centers the metal atom within the octahedron. Sr doping induces more uniform local structural modification with minimal perturbation of valence-band dispersion, thereby avoiding excessive hole effective-mass enhancement. These findings demonstrate that the effectiveness of metal fluoride additives is governed by the interplay between defect energetics, local octahedral distortion, and carrier transport anisotropy, providing a design strategy for efficient and stable lead-free PSCs.

Keywords: Tin perovskite; tin oxidation; metal fluoride additive, defect formation、Sn off-centering.

1. Introduction

Halide perovskite solar cells have rapidly advanced photovoltaic research, achieving power conversion efficiency (PCE) exceeding 27% within a decade. However, these high efficiencies are predominantly realized in lead-based systems, raising environmental and regulatory concerns[1–3]. Tin-based perovskite solar cells (Sn-PSCs) have therefore emerged as promising lead-free alternatives due to their suitable bandgap (≈1.2-1.4 eV), strong optical absorption, low exciton binding energy, and favorable charge-transport properties, making them attractive for both single-junction and tandem applications.[4–6] Despite their potential, the performance of Sn-PSCs lags significantly behind their Pb counterparts, with a record PCE of ≈17% and limited operational stability[7,8]. This limitation primarily originates from the facile oxidation of Sn^{2+} to Sn^{4+}, which induces tin vacancies, severe self-p-doping, high background carrier densities, and enhanced nonradiative recombination losses[9–11]. Additionally, the stereochemically active $5s^2$ lone pair of Sn^{2+} leads to octahedral distortion and local lattice off-centering, creating strain and broad defect states that further compromise defect tolerance. Rapid crystallization results in defective film morphologies[12–15]. These factors severely compromise device efficiency, reproducibility, and operational stability.

To address these challenges, a broad range of strategies has been reported[16,17]. Process engineering approaches, such as reducing atmosphere deposition and solvent coordination control, have mitigated Sn oxidation and improved film morphology[18,19]. Interfacial strategies, including self-assembled monolayers and dipole interlayers, have been developed to reduce interfacial recombination and enhance device stability[20–22]. Apart from these, additive engineering has emerged as one of the most effective routes to enhance the performance of tin-based perovskites[23–26]. Among the various additives, tin fluoride (SnF_2) remains canonical; it suppresses the oxidation of Sn^{2+} to Sn^{4+}, regulates nucleation, and often improves film morphology and optoelectronic quality[27–29]. Consequently, SnF_2 has become a near-ubiquitous component in high-performance tin (and mixed Pb-Sn) absorbers. Recently, Ma et al. reported the use of a bifluoride additive (NH_5F_2) as a substitute for SnF_2 to suppress phase segregation in Sn-perovskite films[30]. The weaker coordination of the $[F–H–F]^-$ anion enabled its removal during annealing, resulting in smoother morphology, reduced defect density, and a record efficiency of 15.04%. Beyond fluorides, broader additive engineering strategies (including antioxidants, Lewis-base/acid complexes, low-dimensional cations, and tailored ligands) have delivered substantial improvements in device efficiency and operational stability[31–33]. In

parallel, cation-doping approaches have recently gained attention for their ability to mitigate defect densities and counteract lone-pair-induced distortions[34–37]. Phung et al. demonstrated that low levels of alkaline-earth dopants can be incorporated into halide perovskite lattices to tune their doping character[37]. Building on this, a recent study on partial substitution of A- or B-site cations in tin perovskites with alkaline-earth elements (e.g., Sr^{2+}) has shown significant reductions in self-p-doping, effective healing of Sn vacancies and off-centering, and relaxation of local lattice strain, collectively leading to lower defect densities and measurable improvements in V_{OC} and fill factor[38]. Although significant improvements have been achieved, most efforts focus either on SnF_2-based additives or on iodide salts of alkaline-earth and rare-earth metals. However, systematic studies exploring the role of fluoride-based salts beyond SnF_2, such as alkaline-earth and rare-earth fluorides, remain scarce despite the unique dual functionality. Fluoride anions can strongly coordinate with Sn^{4+} species and undercoordinated lattice sites, thereby suppressing oxidation and passivating traps[39]. A larger cation may occupy interstitial/vacancy sites, relieve lattice strain, and further stabilize the perovskite structure. Moreover, lanthanide fluorides have been shown in Pb-based systems to interact with solvents such as DMSO, mediating controlled crystallization and yielding enhanced film quality and device durability[40]. Translating these insights to Sn-based systems presents an attractive but largely unexplored pathway.

Motivated by the dual considerations of (i) the well-established ability of fluoride anions to suppress Sn(II) oxidation and passivate electronic trap states, and (ii) the beneficial role of larger cations in reducing vacancy-driven lattice distortion, we introduce metal fluoride (MF_x : BaF_2, SrF_2, and YbF_3) additives for Sn-PSCs. This study explores the mechanistic role of MF_x additives in regulating crystallization, carrier dynamics, and defect physics. Through combined experimental and theoretical analysis, it is demonstrated that these fluoride salt additives enhance film quality, reduce trap-assisted recombination, and improve both efficiency and operational stability compared to control devices. By integrating fluoride chemistry with lattice-stabilizing cations, this work provides a framework for additive engineering in Sn-halide perovskite (Sn-HP) and insights into addressing defect- and stability-related challenges.

2. Results and discussion:

2.1. Effect of binary metal fluoride on Sn-perovskite film properties

The design concept of using metal fluoride (MF_x) additives to stabilize Sn-HPs is demonstrated schematically in Fig. 1a. It conveys the plausible dual action of the additive: (i) the highly electronegative fluoride anion coordinates to undercoordinated Sn^{2+}/Sn^{4+} and passivates V_{Sn}

vacancies, suppressing oxidation; and (ii) the metal cation (M^{2+}) is shown incorporated at/near the Sn site in the octahedron, where it suppresses Sn off-centering and provides local structural reinforcement.

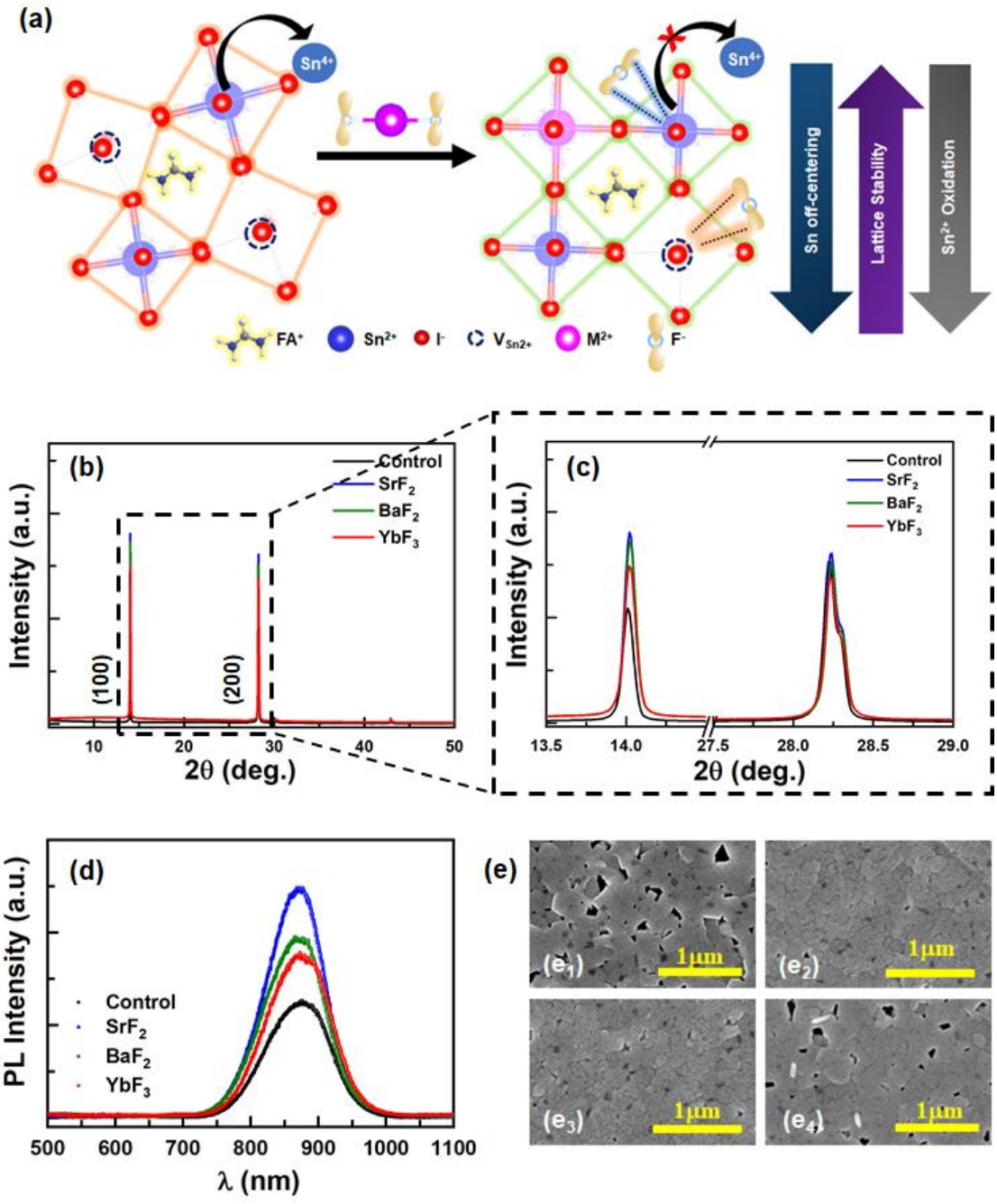

Figure 1. (a) Schematic illustration of metal fluorides and perovskite lattice interaction. (b,c) XRD Patterns with zoomed view. (d) PL spectra. (e) SEM images of Sn-Hp films without and with MF_x additives ((e_1) control, (e_2) SrF_2, (e_3) BaF_2, and (e_4) YbF_3).

Figure 1b presents the X-ray diffraction (XRD) patterns of control Sn-HP films and those prepared with MF_x (BaF_2, SrF_2, and YbF_3) additives. All films exhibit the characteristic diffraction peaks corresponding to the (100) and (200) planes of the 3D perovskite phase[26]. A noticeable enhancement in the diffraction peak intensities (Fig. 1c) is observed for the Sn-HP film with MF_x additive compared to the control, with the most pronounced increase observed for the SrF_2-additive. This intensity enhancement suggests improved crystallinity and a higher degree of preferred orientation along the (100) direction, which is commonly associated with improved charge transport in Sn-HP films[25]. Further, the magnified XRD patterns reveal a slight narrowing of the diffraction peaks for the additive-treated films. It is consistent with improved crystallinity and a possible reduction of microstrain[41]. In Sn-HPs, microstrain is associated with local lattice distortions arising from Sn off-centering[39]. Therefore, the MF_x additive could contribute to improved crystallization and reduced local disorder.

Figure 1d exhibits the steady-state photoluminescence (PL) spectra of control and MF_x additive Sn-HP films. All samples exhibit a single emission peak centered around 875 nm (1.417 eV)[25]. Sn-HP films with binary fluoride show an enhancement in PL intensity, with the SrF_2 films exhibiting the strongest emission. It suggests that the introduction of MF_x additives effectively suppresses nonradiative recombination. The additives are successfully aiding in reducing defect density and improving the electronic quality of the perovskite films. Notably, the emission peak position remains nearly unchanged across all samples (Fig. S1), suggesting that no significant compositional alteration of the perovskite lattice is detectable from PL characteristics. The role of MF_x additives thus appears primarily linked to defect passivation rather than bandgap modification.

Figure 1e shows the top-view scanning electron microscopy (SEM) images of Sn-HP films. The control film exhibits a relatively rough surface morphology with irregularly shaped grains, pinholes, and poorly connected grain boundaries. Such morphological features are known to act as preferential sites for defect formation, moisture ingress, and nonradiative recombination[39]. The Sn-HP film with the MF_x additive shows improved surface coverage and grain uniformity. These SEM images modulated with MF_x additives improve film morphology through chemically mediated regulation of crystallization and interfacial bonding. It can be rationalized by considering the chemical interactions introduced by the fluoride-based additives during film formation[39,42].

2.2. Photovoltaic properties of Sn-PSCs with binary metal fluoride additive

To evaluate the impact of MF_x additives on the photovoltaic performance of Sn-PSCs, devices were fabricated using the architecture ITO/PEDOT:PSS/Sn-HP/ICBA/BCP/Ag. The cross-sectional SEM images of the device (Fig. 2a,b) depict that the SrF_2-additive device forms a more compact columnar growth with improved interfacial contact to the underlying PEDOT:PSS, indicating enhanced film formation and structural integrity compared to the control. Figure 2c shows the current density-voltage (*J-V*) characteristics of Sn-PSCs with MF_x additives measured under AM 1.5G illumination, while the corresponding photovoltaic parameters extracted from multiple devices are summarized in Table 1. The control Sn-PSC exhibited a PCE of ≈9.74%, whereas devices incorporating MF_x additives demonstrated superior PCE. Particularly, the device with SrF_2 additive showed the best PCE of 12.68%. This improvement is accompanied by a notable increase in V_{OC} from ~0.786 V in the control device to ≈0.869 V for SrF_2-based devices, along with a simultaneous enhancement in fill factor (≈ 64 to 71) and J_{SC} (≈19.34 to ≈20.41 mA cm^{-2}). It is attributed to the improved film compactness, reduced defect-assisted recombination at grain boundaries, and more uniform perovskite coverage enabled by the incorporation of fluoride additives, as observed in SEM and PL measurements. Notably, while YbF_3-treated devices exhibit competitive *J*sc values, their slightly reduced *V*oc compared to SrF_2-treated devices suggests subtle differences in defect compensation and the electronic landscape introduced by the aliovalent Yb^{3+} species.

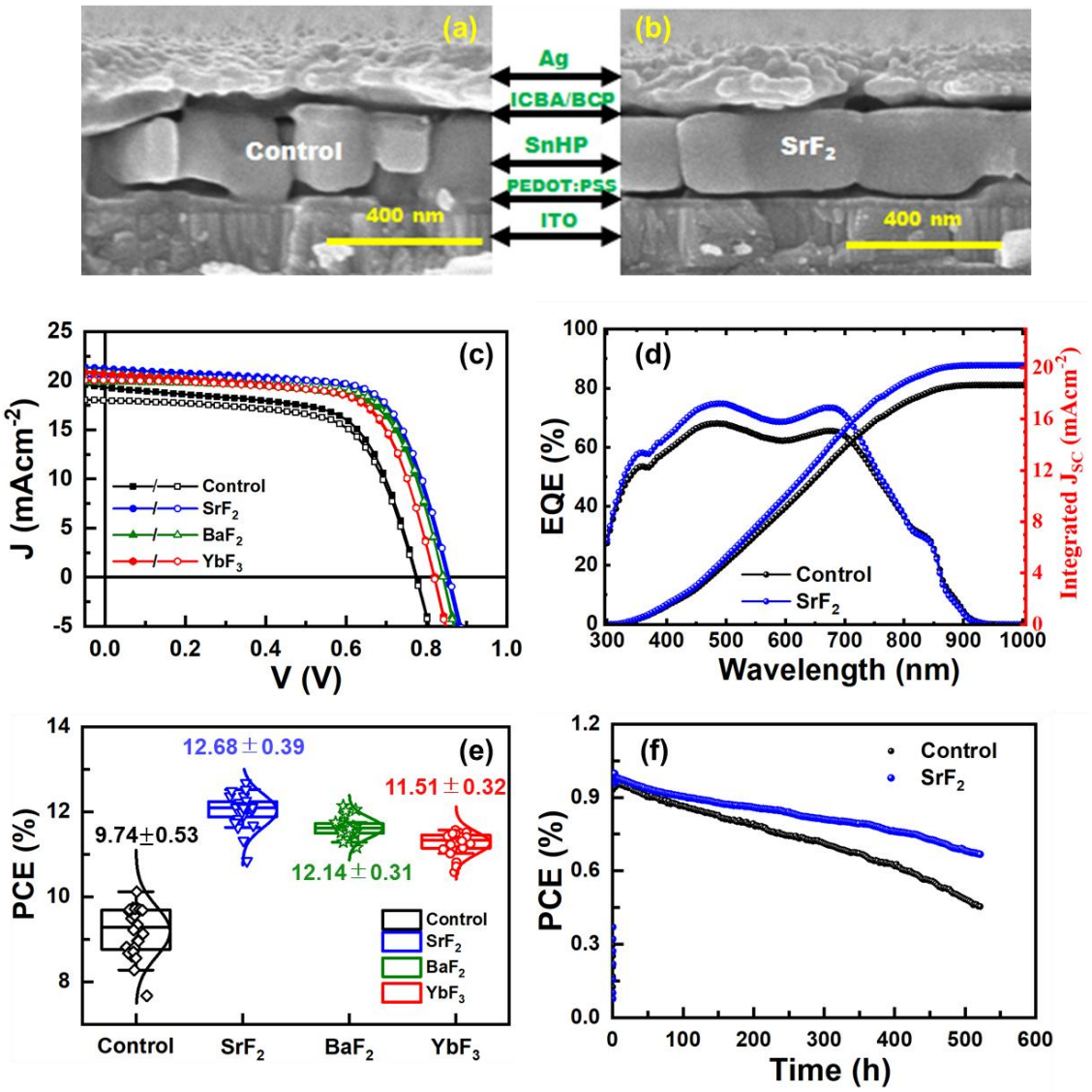

Figure 2. Cross-sectional SEM image of (a) control and (b) SrF_2 additive Sn-PSCs, (c) *J-V* curves of Sn-PSC devices (■ forward/□ reverse scan direction) (control and additives), (d) EQE spectra, (e) statistics of PCE, and (f) operational stability of PSCs under MPPT conditions.

Table 1. Summarized device parameters of the Sn-PSCs without and with fluoride additive. The best device parameters are given outside the parentheses. The average values of PCE and standard deviation (SD) (24 devices from 4 batches).

Device	Scan	J_{SC} ($mAcm^{-2}$)	V_{OC} (V)	*FF*	*PCE* (%)	PCE (Average) ± SD
Control	F	19.34	0.786	0.642	9.74	9.19 ± 0.53
	R	18.01	0.783	0.657	9.25	
SrF_2	F	21.2	0.850	0.684	12.36	12.03 ± 0.39
	R	20.41	0.869	0.715	12.68	
BaF_2	F	20.46	0.846	0.672	11.63	11.62 ± 0.31
	R	19.86	0.845	0.723	12.14	
YbF_3	F	21.04	0.817	0.667	11.46	11.26 ± 0.32
	R	20.32	0.815	0.695	11.51	

Figure 2d presents the external quantum efficiency (EQE) spectra of devices. The device with SrF_2 additive exhibits a consistently higher EQE across a broad spectral range. This enhancement suggests more efficient carrier extraction at the interfaces, as well as improved charge transport and collection within the perovskite bulk[43]. The integrated J_{SC} values calculated from the EQE spectra are 18.65 and 20.21 mA cm^{-2} for the control and SrF_2-additive devices, respectively. This closely matches the corresponding values extracted from the *J-V* curves. In addition, the band edge derived from the EQE onset (Fig. S3) yields an optical bandgap ≈1.410 ± 0.02 eV for the control device and ≈1.416 ± 0.02 eV for the SrF_2-treated device. These values are in good agreement with the band edge obtained from the characteristic PL spectra. The blue shift of bandgap observed for the Sn-HP film with SrF_2- additive is likely associated with reduced band tailing and energetic. These results underscore that the improved device performance mainly arises from reduced recombination losses and more efficient charge collection enabled by the fluoride additive.

To assess reproducibility, a statistical analysis was conducted on 24 devices from 4 batches (Fig. 2e, Fig. S2, and Table S1). The control devices show a broad distribution of efficiencies, centered at 9.19 ± 0.53%. Sn-PSCs with fluoride additives consistently raise the mean efficiency and narrow the distribution range. Among them, SrF_2 exhibits a superior PCE of 12.03 ± 0.39%, while BaF_2 and YbF_3 devices achieve PCE of 11.62 ± 0.31 % and 11.26 ± 0.32%, respectively. The reduced spread in device PCE suggests that fluoride additives promote more uniform film formation and minimize batch-to-batch variability.

Moreover, Figure 2f compares the operational stability of encapsulated control and SrF_2-additive Sn-PSCs measured under continuous maximum power point tracking (MPPT) conditions. The control device undergoes a comparatively faster degradation, retaining only ~50% of its initial PCE after ~500 h of operation. The SrF_2-additive device demonstrates a slower degradation, maintaining approximately ~70% of its initial efficiency over the same time span. The incorporation of SrF_2 likely suppresses defect-mediated degradation pathways by passivating Sn-related deep trap states and stabilizing grain boundaries[44–46]. Additionally, fluoride-based additives may enhance the structural robustness of the Sn-HP lattice by reducing local lattice distortions[38], which will be discussed in more detail later.

2.3. Photo-characteristics of Sn-PSCs with binary metal fluoride additive

To elucidate the recombination dynamics in the control and SrF_2-additive devices, light-intensity-dependent open-circuit voltage (V_{OC}) measurements were performed, as shown in Fig.

3a. For the control device, the slope of the V_{OC} versus natural logarithm of light intensity (lnI) yields a diode ideality factor of $n \approx 2.67 k_B T/q$. It is known that the ideality factor of $n \approx 1$ indicates predominantly band-to-band recombination, while $n \approx 2$ indicates Shockley-Read-Hall (SRH) trap-assisted recombination[47]. It has been reported that the n can vary between 1 and 3 for PSCs, depending on the extent and nature of trap-assisted recombination. Although classical diode theory bounds $1<n<2$, the ideality factors exceeding $n>2$ are reported in PSCs. These high values are attributed to interface-dominated recombination, mobile-ion screening, and combined bulk/ interface trap -assisted recombination pathways[48]. Thus, the pronounced decrease of $n \approx 1.49$ $k_B T/q$ with the SrF_2 additive therefore indicates effective suppression of trap-assisted non-radiative recombination[49].

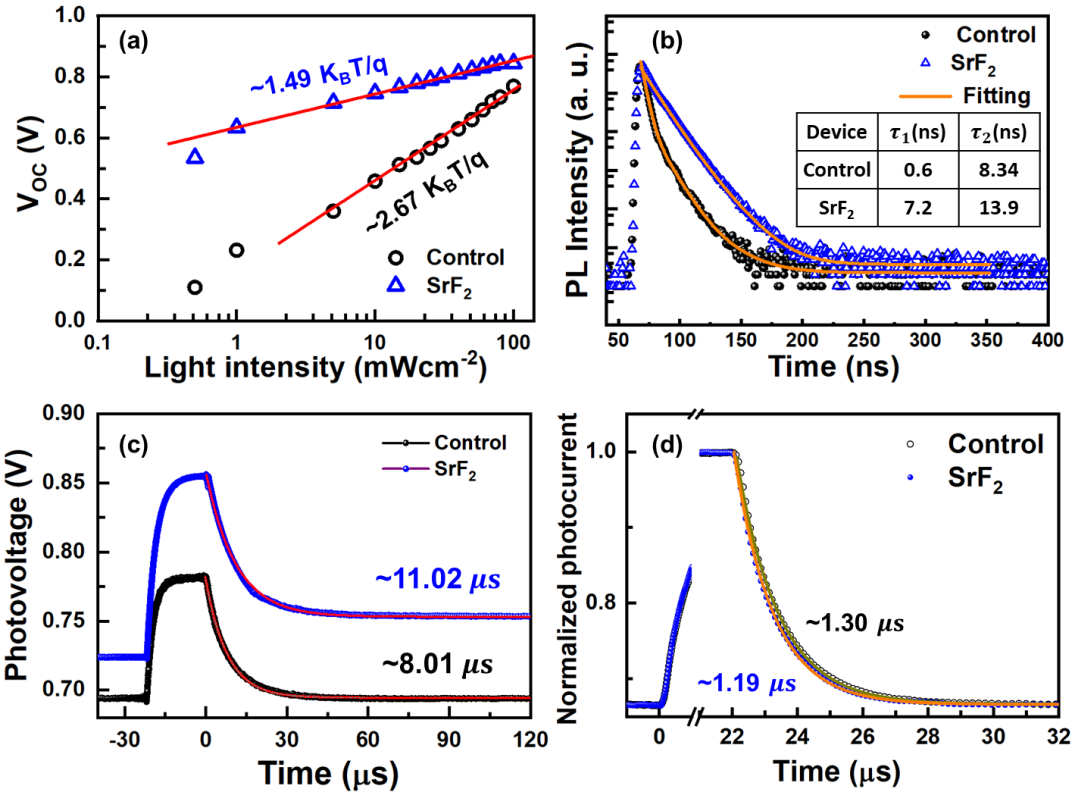

Figure 3. (a) Light intensity dependence of V_{OC}, (b) TRPL data, (c) TPV decay curves, (d) TPC curves of control and SrF_2 additive devices.

The PL decay curves and bi-exponential fitting results are shown in Fig. 3b, with the extracted lifetime in the inset table. The control film exhibits shorter lifetime components ($\tau_1 \approx 0.6$ ns and $\tau_2 \approx 8.34$ ns) compared to the SrF_2-additive film ($\tau_1 \approx 7.2$ ns and $\tau_2 \approx 13.9$ ns). For polycrystalline perovskite films, the fast component τ_1 is associated with trap-mediated non-radiative recombination at surfaces and grain boundaries, whereas the slow component τ_2

reflects radiative/bulk recombination[50]. The marked increase of τ_1 thus indicates effective passivation of surface and grain-boundary traps, leading to a marked suppression of nonradiative recombination pathways, while the longer τ_2 indicates improved bulk carrier lifetime, reflecting reduced defect density and improved lattice stability throughout the perovskite film. These results corroborate the significance of the MF_x additive in improving the performance of Sn-PSCs.

Transient photovoltage (TPV) measurements were performed to further probe the recombination dynamics under open-circuit conditions for the control and SrF_2-treated devices (Fig. 3c). Upon small-perturbation illumination, the SrF_2-additive device (≈11.02 μs) exhibits a prolonged photovoltage decay compared to the control (≈8.01 μs). The longer TPV lifetime for the SrF_2 device indicates a reduced charge recombination rate and a higher density of long-lived charge carriers under operating conditions. This behavior is consistent with suppressed nonradiative recombination pathways, particularly those associated with Sn^{4+}-related deep traps and interfacial defects[25,51].

Transient photocurrent (TPC) measurements were carried out to investigate the charge extraction dynamics and carrier transport efficiency[52,53]. The Sn-PSCs with SrF_2 additive exhibit a noticeably faster photocurrent decay (1.19 μs) compared to the control device (1.30 μs) (Fig. 3d), indicating more efficient charge extraction and reduced carrier trapping. The shorter TPC decay time in the SrF_2-treated device reflects accelerated carrier transport through the perovskite layer and across the interfaces. The complementary TPV-TPC behavior clearly demonstrates that SrF_2 additive simultaneously prolongs carrier lifetimes while enabling rapid charge extraction. This signifies reduced trap density and improved interfacial energetics.

2.4. Modulation of surface chemistry and energy on Sn-HP with metal fluoride additive

To study the surface energy modulation of Sn-HP films, ultraviolet photoelectron spectroscopy (UPS) measurements were performed. Energy-level diagrams were extracted as given in Fig. 4a-d. The control Sn-HP film exhibits a work function (φ) of ≈4.38 eV, with the Fermi level located close to the valence band maximum ($\Delta E_{F,V} \approx 0.62$ eV), indicating strong p-type self-doping and Sn-related acceptor defects arising from partial Sn^{2+} oxidation[38]. Upon incorporation of SrF_2, the work function increases to ≈4.42 eV, and the Fermi level shifts significantly toward the mid-gap region ($\Delta E_{F,V} \approx 0.82$ eV), indicating a substantial suppression of excessive p-type doping and a transition toward a more intrinsic electronic character. Similar trends are observed for BaF_2- and YbF_3-treated films (Fig. S4). The energy level diagrams of

the Sn-HP films with MF_x (Fig. 4c, Fig. S5) were extracted from UPS results. The Sn-HP with SrF_2 additive exhibits a modified electronic structure compared to the control film. The valence band maximum of the SrF_2-additive Sn-HP film got shifted from -5.00 eV (control) to ≈-5.24 eV, closely matching the HOMO level of PEDOT:PSS (≈-5.25 eV). This near-ohmic alignment is expected to promote efficient hole transport and suppress interfacial recombination. The CBM of the Sn-HP with SrF_2-additive (≈-3.82 eV) introduces a conduction band offset of ~0.06 eV relative to the LUMO level of ICBA (≈-3.74 eV) (Fig. 4d). Such a spike has been widely reported to be beneficial in suppressing electron back-transfer and interfacial recombination[54]. It highlights that SrF_2 additives modulate the interfacial energy of Sn-PSCs, enabling efficient charge extraction and recombination suppression. These results also support the increase in device parameters and operational stability.

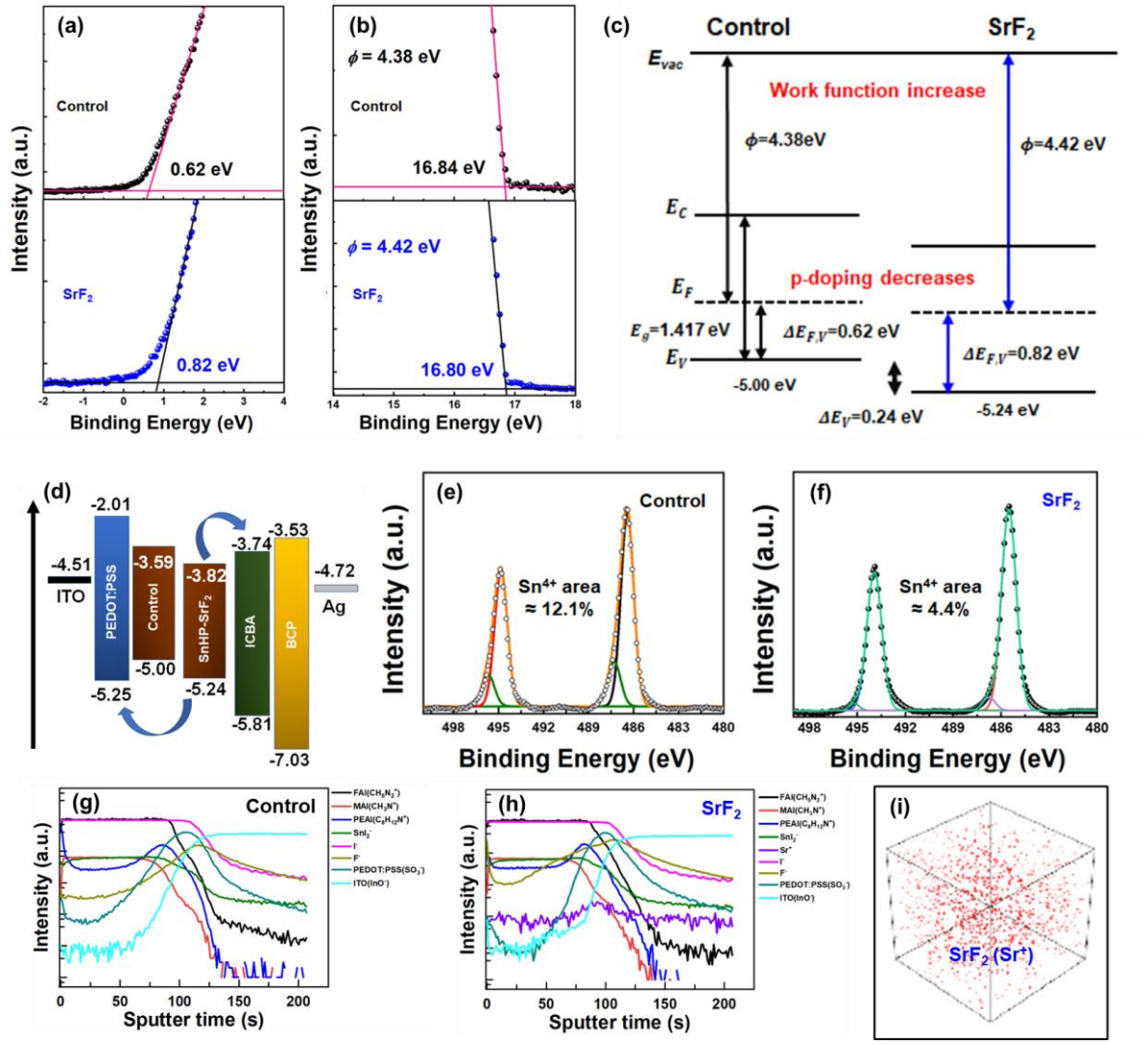

Figure 4. UPS analysis of Sn-HP films. (a) onset energy spectra. (b) secondary electron cutoff spectra, (c) corresponding schematic energy levels, and (d) Device energy band diagram constructed from experimental results. (e,f) XPS: Sn 3d ($3d_{5/2}$ and $3d_{3/2}$) spectra of the Sn-HP

film surfaces without and with SrF_2 additive. ToF-SIMS depth profiles (g) control and (h) SrF_2 -additive Sn-HP film, (i) SrF_2 (Sr^{2+}) distribution 3D images reconstructed from ToF-SIMS depth profiles.

To further investigate the impact of MF_x additives on the surface chemistry, we collected X-ray photoelectron spectra (XPS) of the Sn-HP. Figure 4e-f shows the high-resolution Sn 3d core-level spectra. From the quantitative deconvolution of Sn $3d_{5/2}$ and Sn $3d_{3/2}$, Sn^{4+} component accounts for ~12.1% for the control film. The Sn^{4+} state in Sn-HP with SrF_2 additive is reduced to ~4.4% while that for BaF_2- and YbF_3-additive exhibit Sn^{4+} fractions of ≈4.8 and ≈5.5%, respectively (Fig. S6). This result confirms the effectiveness of MF_x additives in suppressing Sn^{2+} oxidation[26]. The distinct Sn^{4+} fractions among the additives indicate that fluoride passivation alone does not fully account for the observed differences in chemical stabilization and device performance.

To investigate the chemical depth distribution and interfacial characteristics of the perovskite films, ToF-SIMS depth profiling was carried out on control and MF_x additive Sn-HP film deposited on PEDOT:PSS/ITO (Fig.4g,h and Fig. S7). The distribution profiles of key elements show well-confined layers in Sn-HP film with additives. We noticed an enhanced fluoride signal near the perovskite/HTL interface, indicating preferential accumulation of fluoride species at this chemically sensitive region (Fig.S8). These 3D- reconstructed images derived from the ToF-SIMS data further confirm that fluoride-rich regions extend along the perovskite surface and interfacial zones rather than being uniformly distributed throughout the bulk. Such spatial localization of fluoride is favourable for passivating undercoordinated Sn^{2+} sites and chemically active defect centers, thereby limiting Sn oxidation and suppressing defect-assisted recombination. The 3D distribution of Sr^{2+} within the SrF_2-doped perovskite film (Fig. 4i) reveals a homogeneous dispersion of Sr throughout the bulk of the film, confirming uniform incorporation of the additive rather than surface segregation. These results suggest that fluoride additives contribute not only to bulk defect regulation but also play a crucial role in stabilizing the perovskite/HTL interface by mitigating interfacial mixing and chemical degradation.

2.5. Defect analysis of Sn-PSCs with metal fluoride additive

To further probe defect-related charge storage and interfacial polarization effects, capacitance–frequency (*C-f*) measurements were carried out for the control and SrF_2-treated devices (Fig. 5a). At low frequencies ($<10^2$–10^3 Hz), the control device exhibits a relatively higher capacitance than Sn-HP with SrF_2 additive. It is attributed to suppression of trap-assisted

charge storage and diminished ionic or interfacial polarization effects in Sn-PSCs with SrF_2 additive [55,56].

To gain insight into the defect-related charge characteristics of the devices, capacitance spectra were analysed[57,58]. The carrier profile was obtained by the following relation:

$N_{CV} = -\frac{2}{q\varepsilon_0\varepsilon_s}\left[\frac{d}{dV}\left(\frac{1}{C(V)^2}\right)\right]^{-1}$, where N_{CV} represents carrier density calculated from the capacitance-voltage (C-V) curve, C is the capacitance per unit area, ε_0 is the permittivity of free space, ε_s is the dielectric constant of the perovskite material.

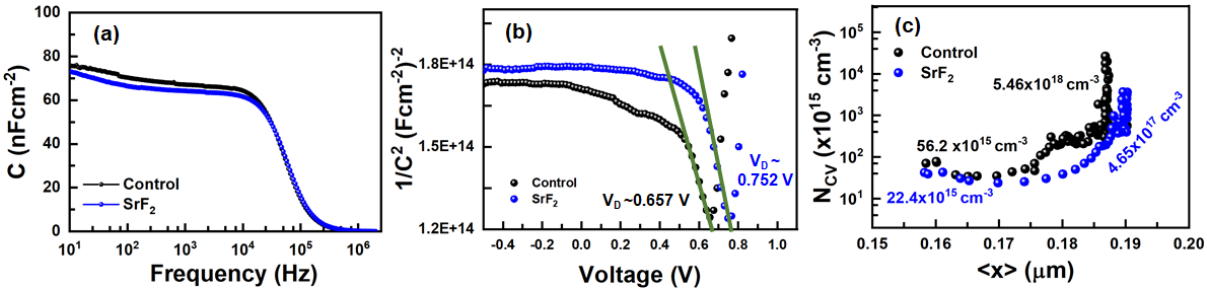

Figure 5. Capacitance characteristics of devices: (a) C-f spectra under dark, (b) Mott-Schottky plots, (c) carrier profile of control and SrF_2 additive devices.

Mott-Schottky plots (Fig. 5b) show an increase in the diffusion potential (V_D) from ~0.657 V (for the control device) to ~0.824 V for the SrF_2-additive device. This aligns with the increase in the V_{OC} of devices. Furthermore, Fig.5c profiles the spatial variation of carrier density across the active layer calculated from C-V measurements. The bulk carrier density in control devices (~5.62×10^{16} cm^{-3}) is attenuated in the SrF_2-aadditive device (~2.24×10^{16} cm^{-3}), indicating a reduced bulk defect density. Similarly, the control device exhibits a relatively high carrier density (~5.46×10^{18} cm^{-3}) compared to the SrF_2-additive device (~4.65×10^{17} cm^{-3}) at the interface, indicating a high interfacial defect density[23]. This reduction in defect density suggests that SrF_2 is effective in the passivation of bulk and interfacial defects. These results support the enhanced carrier lifetimes, reduced nonradiative recombination losses, and improved photovoltaic performance observed in the SrF_2-based devices.

Thus, the performance trend (SrF_2> BaF_2 > YbF_3) is governed by the coupled roles of fluoride ions and their associated metal cations in modulating the chemistry of the Sn-HP absorber. Fluoride ions selectively coordinate with undercoordinated Sn^{2+} at surfaces and grain boundaries, mitigating oxidation and defect formation. Their effectiveness, however, depends

on the accompanying cation. The higher ionic character and lower lattice energies of SrF_2 and BaF_2 facilitate greater fluoride availability during film formation, whereas YbF_3 is limited by its aliovalent nature and restricted fluoride release. This work corroborates that MF_x additives enhance device PCE by concurrently suppressing defect-assisted self-doping, improving crystallization, and optimizing interfacial energetics, with SrF_2 exhibiting the most favorable balance of these effects.

2.6. Theoretical insights into Sn-site doping induced by MF_x additives

To gain deeper theoretical insights, we carried out a comprehensive analysis using Density Functional Theory (DFT) calculations[38,59–61]. To examine Sn-site doping in $FASnI_3$, Sr-, Ba-, and Yb-substituted models were constructed by replacing one Sn atom, as shown in Fig. 6a (Fig. S9-11). The DFT "doping" models represent the microscopic limiting case of Sn-site substitution by the additive cation, while the salts are introduced experimentally as additives. Structural projections reveal that pristine $FASnI_3$ exhibits off-centering of Sn and FA, along with octahedral tilting. We found that doping reduces off-centering with a dopant-dependent effect. Ba induces a larger local distortion. Yb yields a more centered and distinct distortion pattern. Sr shows intermediate behavior with partial suppression of off-centering. This observation is also evident from the comparison of the octahedral volumes as summarized in Table S2. The Octahedral volume analysis shows uniformity in $FASnI_3$, while doping introduces disparities between dopant-centered and neighboring octahedra. Ba- and Sr-induce significant local expansion, whereas Yb- doping causes comparatively smaller volume variation. This variation can also be attributed to differences in the ionic radii of the dopants, as given in Table S3. Accounting for Shannon's effective ionic radii, Ba^{2+}, being larger than Sn^{2+}, induces the most pronounced octahedral expansion, while the smaller Yb^{3+} leads to only minor volume changes. Although Sr^{2+} has a radius comparable to Sn^{2+}, it still shows noticeable expansion, indicating that factors beyond ionic size, such as lattice relaxation and local coordination rearrangement, also play an important role.

Furthermore, local structural distortions were quantified using I-M-I (intra-octahedral), M′-I-M (linkage/tilting), dihedral (twisting), and off-centering displacement metrics (Fig. S11, Table S4-6) to provide a comprehensive view of dopant-induced effects. We found that Sr doping introduces relatively mild and nearly isotropic structural changes. This is evidenced by near-ideal intra-octahedral I-Sr-I bond angles (89.00-91.50°) and reduced off-centering, indicating partial structural stabilization. In contrast, Ba doping leads to pronounced octahedral expansion and strong anisotropy in the inter-octahedral M′-I-M angles (85.26-96.45°), reflecting

significant directional modulation of local tilting and lattice perturbation. In the Yb-doped system, the metal atom is located close to the octahedral center, showing minimal off-centering, whereas the intra-octahedral I-Yb-I bond angles vary widely (81.98-98.95°), indicating pronounced angular distortion within the octahedron. These results underscore distinct structural distortion mechanisms of B-site doping in the $FASnI_3$ system. From the detailed analysis of structural distortion and off-centering displacement, it is corroborated that Ba-doping causes significant octahedral expansion and anisotropic tilting. Yb-doping induces a strong angular distortion with minimal off-centering. While Sr -doping leads to moderate and relatively uniform structural distortions.

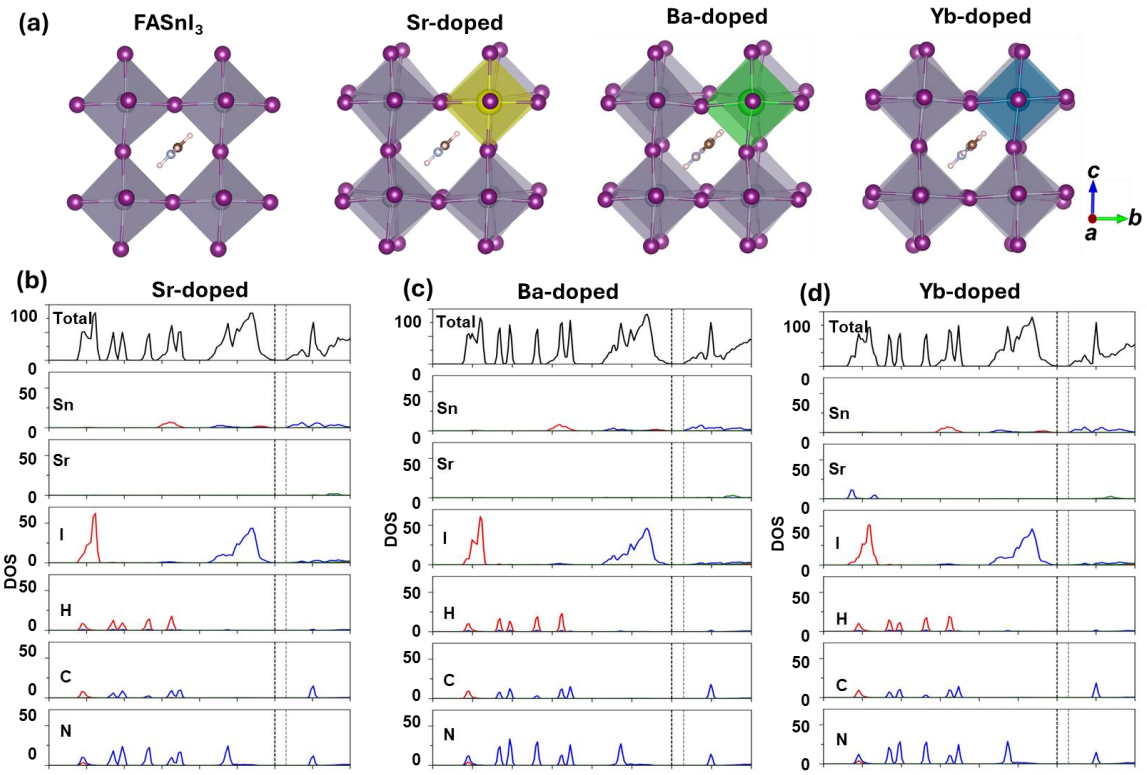

Figure 6. Optimized crystal structures viewed along the a-axis: (a) control, Sr-, Ba-, and Yb-doped in $FASnI_3$. Total density of states (DOS) and partial density of states (PDOS) of (b) Sr-, (c) Ba-, and (d) Yb-doped systems. The black line represents the total density of states, and the red, blue, and green lines represent the s-, p-, and d-orbital-projected densities of states, respectively.

Furthermore, to evaluate the stability of Sn-site doping, it was modeled as antisite substitutional defects (M_{Sn}, where M=Sr, Ba, Yb), in which a dopant atom replaces a Sn atom in the lattice[36,38]. The calculated defect formation energies, which give thermodynamic favourability of defect formation relative to the pristine $FASnI_3$. It shows that the defect formation energies for all

dopants are negative (Table S7), indicating that their incorporation is thermodynamically favorable under the chemical potential conditions used in this calculation. Among them, Ba_{Sn} exhibits the lowest formation energy, suggesting that Ba substitution is the most energetically stable and most likely to occur among the considered dopants.

We also evaluated the effect of dopant on VBM and CBM from the calculated results (Fig. S12). It shows that Sn-site doping primarily alters the absolute energy levels of the CBM and VBM, leaving the band gap nearly unchanged. This indicates that the overall electronic structure is preserved, but the energy alignment of the bands relative to the vacuum level or Fermi level is modulated. These energetic shifts arise from dopant-induced changes in the local electronic environment and orbital interactions. This observation is in line with the experimental UPS results. Importantly, such tunability of band-edge positions, without compromising the band gap, is highly advantageous for band alignment engineering. It enables better matching with charge transport layers and electrodes, thereby improving charge injection and extraction in device architectures.

We further examine how local structural changes are reflected in the electronic states through variations in the effective mass. As summarized in Tables S8 and S9, pristine $FASnI_3$ exhibits pronounced anisotropy at the CBM, whereas Sn-site doping reduces both the electron effective mass and its anisotropy, resulting in more isotropic electron transport. In contrast, the VBM shows a stronger dependence on the dopant species. Sr doping preserves a relatively low hole effective mass along all directions, indicating more balanced carrier transport. Conversely, Ba and Yb doping increase the hole effective mass along specific directions due to valence band flattening. In addition, the band structures (Fig. S13) are consistent with the effective mass trends in Table S9. It is found that Sr doping induces relatively smooth band dispersion with minimal flattening near the band edges, indicating only moderate changes. In contrast, Ba and Yb doping introduce noticeable band flattening near the VBM along specific directions, with the effect being strongest for Ba. This trend aligns with the increased hole effective mass observed in Ba- and Yb-doped systems. These results suggest that Sn-site doping shifts the dominant anisotropy from electrons to holes to some extent.

Figure 6b-d presents the total density of states (DOS) of the doped Sn-HP system. It shows that the DOS profile for Sr-doping results in smooth features near the band edges, whereas Ba and Yb exhibit more pronounced changes, especially near the VBM, due to stronger local distortion. DOS analysis confirms that VBM originates from Sn-s/I-p hybridization and CBM from Sn-p

states, with doping primarily altering the valence band characteristics. This is consistent with band dispersion results, where Sr preserves band curvature with low hole effective mass, while Ba and Yb induce VBM flattening, increasing hole effective mass (m_h^*: Ba > Yb > Sr) particularly along the Γ→Z and Γ→A₀ directions. Thus, Sn-site doping mainly impacts the VBM and hole transport, with Ba and Yb causing stronger anisotropy than Sr.

From a photophysical perspective, all systems exhibit similar absorption onsets (Fig. S14), confirming that Sn-site doping does not significantly alter the band gap. This is consistent with experimental results. However, Sn-site doping exhibits an absorption spectral profile that reflects changes in orbital hybridization and electronic structure. These effects are more pronounced for Ba- and Yb-doped systems, consistent with their stronger structural distortions and impact on the VBM.

Thus, the theoretical analysis of Sn-site doping in $FASnI_3$ provides a versatile route to tune multiple properties simultaneously, including defect stability, band alignment, carrier transport- particularly hole transport, and optical response. These calculations suggest that Sn-site substitution by Sr, Ba, and Yb can modulate the local structure, electronic structure, and optical response of $FASnI_3$. These trends may help rationalize the improved photovoltaic performance observed in the corresponding Sn-PSCs.

Building on the present results, several complementary strategies could push the device's efficiency beyond the one achieved here. Although the MF_x additives markedly enhance the bulk and interface quality, the champion V_{OC} (≈0.87 V) still exhibits a considerable deficit relative to the ≈1.4 eV bandgap of Sn-HPs, indicating that residual non-radiative recombination in the bulk and at interfaces remains a major loss pathway[30]. Further efficiency gains can therefore be achieved through synergistic surface passivation and interface engineering to suppress interfacial defects and improve energy-level alignment[62]. In addition, optimization of additive concentration and the development of alternative fluoride sources could provide more homogeneous crystallization and reduced defect densities. Combining the bulk modification strategy with advanced charge-transport layers or 2D/3D heterostructure engineering[63] presents a promising route for state-of-the-art Sn-based PSC efficiencies represents a promising direction. These approaches could further enhance charge extraction, reduce recombination losses, and unlock the full potential of fluoride-engineered Sn-PSCs.

3. Conclusion

This work systematically investigated the role of metal fluoride additives, BaF_2, SrF_2, and YbF_3, whose cations can act as a dilute Sn-site dopant, in $FASnI_3$-based perovskite solar cells. It establishes a dual-channel passivation strategy in which F^- suppresses Sn^{2+} oxidation and passivates V_{Sn} vacancy trap states, while the accompanying metal cations regulate local octahedral structure and electronic properties through Sn-site substitution. Comprehensive material characterization confirms that MF_x additives modulate film crystallization, surface energy, and defect chemistry synergistically. SrF_2 incorporation delivers the most favorable outcome, improving PCE from 9.7% to 12.7% with enhanced operational stability, while the experimentally observed hierarchy ($SrF_2 > BaF_2 > YbF_3$) reflects a balance between competing material requirements that cannot be optimized through ionic size or charge neutrality alone, but must account for the anisotropy of carrier transport and the degree of local octahedral distortion introduced by each dopant. Taken together, these findings shift the design logic for fluoride-based additives from empirical screening toward a property-driven selection framework, where thermodynamic stability, off-centering suppression, and valence band preservation serve as guiding criteria. Extending this framework to different compositions and probing the long-term interfacial behavior of Sn-F interactions under operational stress remains an important direction for consolidating fluoride additive engineering as a reliable strategy for lead-free perovskite photovoltaics.

Supporting Information

Supporting Information is available online or by the author.

AUTHOR INFORMATION

Corresponding author.
*Email:
DBK: KHADKA.B.Dhruba@nims.go.jp
AM: muraokaa@fc.jwu.ac.jp

ORCID

Aman Shukla: 0009-0003-1687-3201
Mai Otake:0009-0000-2725-1895
Masatoshi Yanagida: 0000-0002-8065-7875
Koichi Yamashita: 0000-0002-6226-3194
Azusa Muraoka:0000-0001-8005-0478
Yasuhiro Shirai: 0000-0003-2164-5468
Dhruba B. Khadka: 0000-0001-9134-3890

Author contributions

Aman Shukla: data curation, formal analysis, visualization, investigation, writing- original draft.
Mai Otake: investigation, data curation, visualization.
Masatoshi Yanagida: resources, validation, visualization, supervision, data curation, funding acquisition, project administration, writing-review & editing.
Koichi Yamashita: investigation, data curation, visualization, writing -review & editing.
Azusa Muraoka: investigation, data curation, visualization, writing-review & editing.
Yasihiro Shirai: resources, supervision, methodology, validation, visualization, investigation, formal analysis, data curation, writing-review & editing.
Dhruba B. Khadka: conceptualization, methodology, supervision, validation, visualization, investigation, formal analysis, data curation, writing-review & editing, writing-original draft.

Conflict of interest

The authors declare no competing financial interest.

Acknowledgments

This work was supported by the Hitachi Global Foundation, Kurata grants (#1572), and partially by the JST-ALCA-Next Program (Grant Number JPMJAN23B2), Japan. We also acknowledge the technical support provided by Yamaguchi Kazuo-San (XPS), Takahashi Hiromi (XRD), and Nariaki Sato-San (ToF-SIMS) from the NIMS battery research platform for the technical support for the respective measurements and analyses. AS expresses appreciation to the National Institute for Materials Science (NIMS) for the opportunity to participate in the short-term "NIMS Internship Program." The computation in this work has been done using the facilities of the Supercomputer Center, the Institute for Solid State Physics, the University of Tokyo (ISSPkyodo-SC-2025-Ca-0116, 2024-A-0019). AM acknowledges JSPS KAKENHI (Grant Number 25K08813) and Special Research Funds from Japan Women's University to develop this research project. KY acknowledges JSPS KAKENHI (Grant Number 24K08356). The authors are deeply thankful to Prof. Monica Katiyar and Prof. Kenjiro Miyano for their insightful comments and constructive suggestions in this work.

References

1 M. A. Green, E. D. Dunlop, M. Yoshita, N. Kopidakis, K. Bothe, G. Siefer, X. Hao and J. Y. Jiang, *Progress in Photovoltaics: Research and Applications*, 2026, **34**, 482–496.

2 A. Babayigit, A. Ethirajan, M. Muller and B. Conings, *Nat. Mater.*, 2016, **15**, 247–251.

3 D. B. Khadka, Y. Shirai, M. Yanagida, J. W. Ryan, Z. Song, B. G. Barker, T. P. Dhakal and K. Miyano, *Solar RRL*, 2023, **7**, 2300535.

4 N. K. Noel, S. D. Stranks, A. Abate, C. Wehrenfennig, S. Guarnera, A.-A. Haghighirad, A. Sadhanala, G. E. Eperon, S. K. Pathak, M. B. Johnston, A. Petrozza, L. M. Herz and H. J. Snaith, *Energy Environ. Sci.*, 2014, **7**, 3061–3068.

5 J. Tong, Z. Song, D. H. Kim, X. Chen, C. Chen, A. F. Palmstrom, P. F. Ndione, M. O. Reese, S. P. Dunfield, O. G. Reid, J. Liu, F. Zhang, S. P. Harvey, Z. Li, S. T. Christensen, G. Teeter, D. Zhao, M. M. Al-Jassim, M. F. A. M. van Hest, M. C. Beard, S. E. Shaheen, J. J. Berry, Y. Yan and K. Zhu, *Science*, 2019, **364**, 475–479.

6 F. Hao, C. C. Stoumpos, D. H. Cao, R. P. H. Chang and M. G. Kanatzidis, *Nat. Photonics*, 2014, **8**, 489–494.

7 J. Chen, J. Luo, E. Hou, P. Song, Y. Li, C. Sun, W. Feng, S. Cheng, H. Zhang, L. Xie, C. Tian and Z. Wei, *Nat. Photonics*, 2024, **18**, 464–470.

8 T. Leijtens, G. E. Eperon, N. K. Noel, S. N. Habisreutinger, A. Petrozza and H. J. Snaith, *Adv. Energy Mater.*2015, **5**, 1500963

9 D. Ricciarelli, D. Meggiolaro, F. Ambrosio and F. De Angelis, *ACS Energy Lett.* 2020 ***5*** **(9)**, 2787-2795

10 M. Awais, R. L. Kirsch, V. Yeddu and M. I. Saidaminov, *ACS Mater. Lett.*, 2021, **3**, 299–307.

11 J. Liu, H. Yao, S. Wang, C. Wu, L. Ding and F. Hao, *Adv. Energy Mater.*2023, **13**, 2300696

12 D. H. Fabini, G. Laurita, J. S. Bechtel, C. C. Stoumpos, H. A. Evans, A. G. Kontos, Y. S. Raptis, P. Falaras, A. Van der Ven, M. G. Kanatzidis and R. Seshadri, *J. Am. Chem. Soc.*, 2016, **138**, 11820–11832.

13 D. Di Girolamo, E. Blundo, G. Folpini, C. Ponti, G. Li, M. H. Aldamasy, Z. Iqbal, J. Pascual, G. Nasti, M. Li, R. Avolio, O. Russina, A. Latini, F. Alharthi, M. Felici, A. Petrozza, A. Polimeni and A. Abate, *Solar RRL*, 2022, **6**, 2100825.

14 G. Laurita, D. H. Fabini, C. C. Stoumpos, M. G. Kanatzidis and R. Seshadri, *Chem. Sci.*, 2017, **8**, 5628–5635.

15 M. Yin, H. Yao, H. Qiu, C. Wu, M. Zhang and F. Hao, *Adv. Funct. Mater.* 2024, **34**, 2404792.

16 B. Nakamanya, T. Kakooza, Q. Sun, M. Haghayegh, A. Balilonda, M. Tebyetekerwa, S. Yang and M. Zhu, *J. Mater. Chem. C Mater.*, 2024, **12**, 4184–4207.

17 Z. Zhang, Y. Huang, J. Jin, Y. Jiang, Y. Xu, J. Zhu and D. Zhao, *Angew. Chem. Int. Ed.* 2023, **62**, e202308093.

18 H. Dong, C. Ran, W. Gao, N. Sun, X. Liu, Y. Xia, Y. Chen and W. Huang, *Adv. Energy Mater.*, 2022, **12**, 2102213.

19 T.-B. Song, T. Yokoyama, C. C. Stoumpos, J. Logsdon, D. H. Cao, M. R. Wasielewski, S. Aramaki and M. G. Kanatzidis, *J. Am. Chem. Soc.*, 2017, **139**, 836–842.

20 F. Ali, C. Roldán-Carmona, M. Sohail and M. K. Nazeeruddin, *Adv. Energy Mater.*, 2020, **10**, 2002989.

21 S. Y. Kim, S. J. Cho, S. E. Byeon, X. He and H. J. Yoon, *Adv. Energy Mater.*, 2020, **10**, 2002606.

22 Q. Chen, C. Wang, Y. Li and L. Chen, *J. Am. Chem. Soc.*, 2020, **142**, 18281–18292.

23 D. B. Khadka, Y. Shirai, M. Yanagida and K. Miyano, *ACS Appl. Energy Mater.*, 2021, **4**, 12819–12826.

24 F. Zhang and K. Zhu, *Adv. Energy Mater.,* 2020, **10**, 1902579.

25 D. B. Khadka, Y. Shirai, M. Yanagida, T. Tadano and K. Miyano, *Chemistry of Materials*, 2023, **35**, 4250–4258.

26 A. Shukla, D. B. Khadka, C. Li, M. Rikukawa, Y. Takeoka, R. Sahara, M. Yanagida and Y. Shirai, *J. Mater. Chem. A Mater.*, 2025, **13**, 23487–23498.

27 S. Gupta, D. Cahen and G. Hodes, *The Journal of Physical Chemistry C*, 2018, **122**, 13926–13936.

28 X. Wan, C. Xu, H. Wang, Z. Jiang, F. Li, G. Xu, Z. Dai, X. He and Q. Song, *Small*, 2024, **20**, 2401136.

29 F. Chen, X. Hu, L. Jisi, L. Su, H. Zhao, Y. Wei, R. Zhou, Y. Chen, J. Qu, Y. Xiong, M. Liang and W. Zhang, *Mater. Today Commun.*, 2024, **38**, 108552.

30 M. Ma, X. Jiang, Z. Zang, X. Wen, W. Zhou, H. Wu, S. Peng, Y. Liu, H. Li, D. Yu, H. Liang, H. Wang, W. Zhou, Z. Su, F. Zheng, X. Gao, A. V. Emeline, C. C. Stoumpos and Z. Ning, *Adv. Funct. Mater.*, 2024, **34**, 2407095

31 T. Naito, M. Takagi, M. Tachikawa, K. Yamashita and T. Shimazaki, *J. Phys. Chem. Lett.*, 2023, **14**, 6695–6701.

32 P. Li, X. Cao, J. Li, B. Jiao, X. Hou, F. Hao, Z. Ning, Z. Bian, J. Xi, L. Ding, Z. Wu and H. Dong, *Nanomicro Lett.*, 2023, **15**, 167.

33 D. Yao, M. T. Hoang and H. Wang, *Small Methods*, 2021, **5**, 2001147

34 L. Gregori, C. Frasca, D. Meggiolaro, P. Belanzoni, M. W. Ashraf, A. Musiienko, A. Abate and F. De Angelis, *ACS Energy Lett.*, 2024, **9**, 3036–3041.

35 T. Wang, X. Xu, W. Li, Y. Li, Q. Liu, C. Li, C. Shan, G. Li, T. Shi and A. K. K. Kyaw, *ACS Appl. Energy Mater.*, 2022, **5**, 11191–11199.

36 S. Adjokatse, S. Kahmann, H. Duim and M. A. Loi, *APL Mater.*, 2019, **7**, 31116.

37 N. Phung, R. Félix, D. Meggiolaro, A. Al-Ashouri, G. Sousa e Silva, C. Hartmann, J. Hidalgo, H. Köbler, E. Mosconi, B. Lai, R. Gunder, M. Li, K.-L. Wang, Z.-K. Wang, K. Nie, E. Handick, R. G. Wilks, J. A. Marquez, B. Rech, T. Unold, J.-P. Correa-Baena, S. Albrecht, F. De Angelis, M. Bär and A. Abate, *J. Am. Chem. Soc.*, 2020, **142**, 2364–2374.

38 C. Frasca, P. Alippi, R. Schwiddessen, K. Prashanthan, G. Nasti, S. Zuo, M. Okash Ur Rehman, M. H. Aldamasy, N. T. Putri Hartono, A. Musiienko and A. Abate, *ACS Energy Lett.*, 2025, **10**, 526–533.

39 J. Pascual, M. Flatken, R. Félix, G. Li, S. Turren-Cruz, M. H. Aldamasy, C. Hartmann, M. Li, D. Di Girolamo, G. Nasti, E. Hüsam, R. G. Wilks, A. Dallmann, M. Bär, A. Hoell and A. Abate, *Angew. Chem. Int. Ed.*, 2021, **60**, 21583–21591.

40 Z. Li, Y. Cao, J. Feng, J. Lou, Y. Liu and S. (Frank) Liu, *Small*, DOI:10.1002/smll.202303017.

41 Y. Zhao and J. Zhang, *J. Appl. Crystallogr.*, 2008, **41**, 1095–1108.

42 M. Ma, X. Jiang, Z. Zang, X. Wen, W. Zhou, H. Wu, S. Peng, Y. Liu, H. Li, D. Yu, H. Liang, H. Wang, W. Zhou, Z. Su, F. Zheng, X. Gao, A. V Emeline, C. C. Stoumpos and Z. Ning, *Adv. Funct. Mater.*2024, **34**, 2407095.

43 A. Nakane, H. Tampo, M. Tamakoshi, S. Fujimoto, K. M. Kim, S. Kim, H. Shibata, S. Niki and H. Fujiwara, *J. Appl. Phys.*, 2016, **120**, 064505.

44 S. Zou, S. Ren, Y. Jiang, Y. Huang, W. Wang, C. Wang, C. Chen, X. Hao, L. Wu, J. Zhang and D. Zhao, *Energy & Environmental Mater.*, 2023, **6**, e12465–e12465.

45 A. Abate, *ACS Energy Lett.*, 2023, **8**, 1896–1899.

46 D. B. Khadka, Y. Shirai, M. Yanagida and K. Miyano, *ACS Appl. Energy Mater.*, 2021, **4**, 11121–11132.

47 G. J. W. Aalbers, T. P. A. van der Pol, K. Datta, W. H. M. Remmerswaal, M. M. Wienk and R. A. J. Janssen, *Nat. Commun.*, 2024, **15**, 1276.

48 W.-Q. Wu, Z. Yang, P. N. Rudd, Y. Shao, X. Dai, H. Wei, J. Zhao, Y. Fang, Q. Wang, Y. Liu, Y. Deng, X. Xiao, Y. Feng and J. Huang, *Sci. Adv.2019,* **5**, eaav8925(2019)

49 D. B. Khadka, Y. Shirai, M. Yanagida, T. Masuda and K. Miyano, *Sustain. Energy Fuels*, 2017, **1**, 755–766.

50 D. Cao, Z. Jiao, J. Gao, Y. Wang, X.-C. Ai and J.-P. Zhang, *Nat. Commun.*, 2025, **16**, 11352.

51 D. B. Khadka, Y. Shirai, M. Yanagida, H. Ota, A. Lyalin, T. Taketsugu and K. Miyano, *Nat. Commun.*, 2024, **15**, 882.

52 C. Pramanik, R. Garai, N. P. Jasti, N. Nandi, A. D. Mohite and K. S. Narayan, *Adv. Energy Mater.*,2025,**15**, 2502346.

53 D. B. Khadka, Y.-C. Kuo, Y. Z. Li, M. Waqas, Y.-J. Xu, M. Yanagida, H. Nishihara, K. Tsukagoshi, M. M. C. Chou, Y. Shirai and Y.-C. Wang, *ACS Appl. Mater. Interfaces*, 2025, **17**, 26813–26822.

54 C. Ding, Y. Zhang, F. Liu, Y. Kitabatake, S. Hayase, T. Toyoda, K. Yoshino, T. Minemoto, K. Katayama and Q. Shen, *Nano Energy*, 2018, **53**, 17–26.

55 M. A. Kamarudin, D. Hirotani, Z. Wang, K. Hamada, K. Nishimura, Q. Shen, T. Toyoda, S. Iikubo, T. Minemoto, K. Yoshino and S. Hayase, *J. Phys. Chem. Lett.*, 2019, **10**, 5277–5283.

56 K. Miyano, M. Yanagida, N. Tripathi and Y. Shirai, *J. Phys. Chem. Lett.*, 2016, **7**, 2240–2245.

57 D. B. Khadka, Y. Shirai, M. Yanagida, T. Tadano and K. Miyano, *Adv. Energy Mater.*, 2022, **12**, 2202029.

58 D. B. Khadka, Y. Shirai, M. Yanagida and K. Miyano, *ACS Appl. Mater. Interfaces*, 2019, **11**, 7055–7065.

59 M. Otake, S. Omori, M. Kaneko, M. Palummo, G. Giorgi, K. Yamashita and A. Muraoka, *The Journal of Physical Chemistry C*, 2025, **129**, 18200–18210.

60 D. B. Khadka, Y. Shirai, R. Sahara, M. Yanagida and K. Miyano, *Small*, 22025, **21**, 2410048.

61 M. OTAKE, S. OMORI, S. KOGURE, M. KANEKO, K. YAMASHITA and A. MURAOKA, *Journal of Computer Chemistry, Japan*, 2024, **23**, 2024–0010.

62 J. Chen, J. Luo, E. Hou, P. Song, Y. Li, C. Sun, W. Feng, S. Cheng, H. Zhang, L. Xie, C. Tian and Z. Wei, *Nat. Photonics*, 2024, **18**, 464–470.

63 T. Wang, H. Loi, J. Cao, Z. Qin, Z. Guan, Y. Xu, H. Cheng, M. G. Li, C. Lee, X. Lu and F. Yan, *Advanced Science*, 2022, **9**, 2200242.